

Article

The Symmetry and Stability of the Flow Separation around a Sphere at Low and Moderate Reynolds Numbers

Junwei Li  and Benmou Zhou *

Science and Technology on Transient Physics Laboratory, Nanjing University of Science and Technology, Nanjing 210094, China; ljw89@njjust.edu.cn

* Correspondence: bmzhou@njjust.edu.cn

Abstract: The flow separation state reflects the symmetry and stability of flow around spheres. The three-dimensional structures of flow around a rigid sphere at moderate Reynolds number (Re) between 20 and 400 by using finite volume method with adaptive mesh refinement are presented, and the process of separation angles changing from stable to oscillating state with increasing of Re is analyzed. The results show that the flow is steady, and the separation angles are stable and axisymmetric at Re in less than 200. The flow is unsteady and time-periodic, and the flow separation becomes regular fluctuations and asymmetric at $Re = 300$, which leads to the nonzero value of lateral force and the phase difference between lift and lateral force. At $Re = 400$, the flow is unsteady, non-periodic, and asymmetric, as is the flow separation. It's concluded that the flow separation angle increases when Re increases within a range between 40 and 200. With Re continues to increase, the flow separation state changes from stable to periodically regular until quasi-periodically irregular. The vortex structure changes from no shedding to asymmetric periodic shedding, and finally to asymmetric and intermittently periodic vortex shedding. These results have important implications for the stability of flow around spheres.



Citation: Li, J.; Zhou, B. The Symmetry and Stability of the Flow Separation around a Sphere at Low and Moderate Reynolds Numbers. *Symmetry* **2021**, *13*, 2286. <https://doi.org/10.3390/sym13122286>

Academic Editors: Mikhail A. Sokolovskiy and Xavier Carton

Received: 29 September 2021
Accepted: 23 November 2021
Published: 1 December 2021

Publisher's Note: MDPI stays neutral with regard to jurisdictional claims in published maps and institutional affiliations.



Copyright: © 2021 by the authors. Licensee MDPI, Basel, Switzerland. This article is an open access article distributed under the terms and conditions of the Creative Commons Attribution (CC BY) license (<https://creativecommons.org/licenses/by/4.0/>).

Keywords: flow around a sphere; flow separation; adaptive mesh; force coefficient; vortex shedding

1. Introduction

The incompressible viscous flow around a sphere is important in fluid mechanics [1,2]. There are also many applications in the ocean, such as spherical detectors, spherical buoys, etc. The phenomenon of fluid separated from the spherical surface has been studied by many physicists, engineers, and mathematicians [3,4], and this is attributed to its extensive application in engineering, industrial and environmental flow. Flow stability is important when flow around blunt bodies, and asymmetric flow separation can have a great impact on the stability of the flow. Therefore, it is necessary to study the separation of flow around a sphere from axisymmetric to asymmetric flow separation, which occurs at the Reynolds number between 200 and 400 [5,6]. However, the details of flow separation are not described much with the increase of Reynolds number. In previous literature, people only listed the separation angles and the lengths of the separation bubble under a certain Reynolds number, and they are all fixed values. Of course, these are applicable when the Reynolds number is under 200. However, when the Reynolds number exceeds 270 (the flow is unsteady under this Reynolds number [7]), it is worth thinking about that whether the separation angle is fixed over time at a given Reynolds number.

With the increase of Reynolds number, the wake vortex and symmetry structure of flow around a sphere have been analyzed a lot. Many experiments and simulations have been carried out to figure out that there are various flow regimes that occur for uniform flow around a stationary rigid sphere with increasing Reynolds number. In the literature [5,6], some summaries that the flow mechanisms in wake field were not the same in different Reynolds number intervals were given. Flow separation around a sphere occurs when

the shear stress is zero [8]. The flow separation angle measured from the front stagnation point decreases with the increasing Reynolds number between 20 and 500. It is due to the inertia effects being more dominant than the viscous effect as the Reynolds number increases, and the boundary layer separates from the sphere more quickly. Separation angle measured from the rear stagnation point of steady flow around a sphere at different Reynolds numbers under 375 was discussed [9]. As the Reynolds number gradually increases, the separation angle also gradually increases. Moreover, the growth trend is getting slower and slower. The variation law of the separation angle also appears when the Reynolds number is under 1000 [10]. It is also mentioned in other literature [11] that the variation of the separation angle with time is unstable under a certain Reynolds number, but the authors attribute it to the instability of numerical simulation. Moreover, a new vorticity model is established to characterize the separation of symmetric flow fields [12].

The experiments were conducted mainly by means of the condensed milk method with the flow around a sphere at Reynolds numbers between about 60 and 300. The separation angle also increased with the increasing Reynolds number, and this phenomenon is consistent with the results of numerical simulation [13]. The empirical formula obtained by the experimental method was the functional relationship between the separation angle and the Reynolds number when the Reynolds number was between 30 and 750 [14]. Based on this, a similar modified empirical formula also appears and the Reynolds number was between 300 and 3000 [15]. The experiments of flow past a sphere in wind tunnels have also been performed at Reynolds numbers ranging from 3×10^4 to 3×10^7 with $0.3 \leq Ma \leq 3$ [16]. The effect of the Mach and Reynolds numbers on the position of the separation point was investigated. Additionally, the experimental investigation of the separation process of multi-spheres had been performed in hypersonic flow, and the effects of the number of spheres and the ratio of the diameter on flow separation are investigated [17,18]. Of course, experiments were conducted to study the flow separations of a sphere rolling on an inclined plane at Reynolds number between 1350 and 1550 [19]. Flow separation was divided into four different regions, and each region had different characteristics.

In this paper, the numerical simulation and analysis of flow around a grid sphere at low and moderate Reynolds numbers $20 \leq Re \leq 400$ are performed and the variation of separation angles over time at fixed Reynolds number is on focus. The flow is steady, and the separation angles are stable and axisymmetric at $20 \leq Re \leq 200$. With the Reynolds number increasing continually, the vortex in the flow field and flow separation of flow around the sphere change from regular to irregular flow state.

2. Governing Equations and Numerical Methods

2.1. Problem Description

The whole calculation zone of the flow field is as follows Figure 1, and the computational mesh near the sphere is the right one (Figure 1b). The diameter of the sphere is d and the length of the calculation zone is $60d$. The width and height of the zone are the same value of $10d$. The fluid flows from left to right. The left side and the upper, lower, front, and rear sides of the calculation area are all velocity inlets. The right side is a free outlet boundary condition. The surface of the sphere is in no-slip condition.

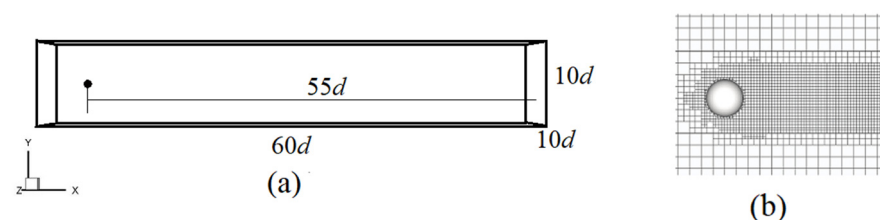


Figure 1. (a) Schematic view and geometrical details of computational domain for flow around sphere; (b) the closed snapshot of boundary layer mesh near the sphere.

2.2. Governing Equations

The incompressible Navier–Stokes equations in non-dimensional form can be written as follows:

$$\nabla \cdot U = 0 \quad (1)$$

$$\frac{\partial U}{\partial t} + U \cdot \nabla U = -\nabla p + \frac{1}{Re} \nabla^2 U \quad (2)$$

In the equations, the non-dimensional variables are obtained like this:

$$U = \frac{U^*}{U_\infty}, t = \frac{U_\infty t^*}{d}, p = \frac{P^*}{\rho U_\infty^2}, Re = \frac{U_\infty d}{\nu} \quad (3)$$

where, U_∞ is the freestream velocity, t^* is the calculating time, U^* and P^* are the velocity and pressure of the flow, ρ and ν are the density and the kinematic viscosity coefficient of the fluid. The superscript * means that the variable is dimensional.

2.3. Numerical Method

The viscous flow solver used is the freely available code Gerris which is described in detail in Popinet [20]. It uses the method of direct numerical simulation (DNS). The domain is discretized by cubic finite volumes organized hierarchically as an octree [20,21]. The tree-type discretization is very flexible and keeps the simple feature of orthogonal discretization volume (Figure 1b). The criterion of local vorticity magnitude is employed in order to adapt the mesh dynamically and follow the evolving turbulent wake [22]. The cubes are dynamically divided based on certain given field parameters

$$\frac{\delta \|\nabla \times U\|}{\max \|U\|} > \varepsilon \quad (4)$$

where, δ is the size of volumes. ε , which is a constant between 0 and 1, represents the threshold limits the maximum vorticity allowed when the fluid microclusters pass through a unit at the maximum velocity. In this paper, ε is set to be 0.01 for all conditions by default. The selection of the local vorticity threshold enables the mesh to adapt dynamically according to the size of the local vorticity and can capture the complex vortex structure in the flow field with small computational complexity.

The second-order time staggered discrete fractional step projection method is used for time dispersion [20], and this projection method depends on the Hodge decomposition of the velocity field. The incompressible N-S equation and continuity equation are solved by finite volume method under the hierarchical grid, and Poisson equation is solved by projection method and multi-grid method. The convection term of the equation is discretized by the second-order upwind Bell–Colella–Glaz scheme, which is stable for a CFL number less than 1. The diffusion term is discretized by the implicit Crank–Nicholson method. It has second-order accuracy and unconditional stability; therefore, both time and space discretization have second-order accuracy.

2.4. Grid Convergence Verification

The size of mesh element has significant impacts on the convergence of the computational simulation results. It is easier to obtain more accurate results in CFD simulation with finer mesh generally. However, the increase in mesh element number give rises to the increase of computer time cost dramatically and reduce the efficiency of the method. In the present study, there are seven different cases of a model named level 5 (the number of cells 504,368), level 6 (580,132), level 7 (677,704), level 8 (724,368), level 9 (816,888), level 10 (918,972), and level11 (1,295,520). All of the above calculations are done with the Reynolds number $Re = 300$ where $\overline{C_d}$ is the time-average coefficient of total drag force. Table 1 shows the error percentages of drag coefficient between other grid levels and 11 grid level, and the result of level 10 can guarantee a relatively stable result compared with that of level 11. Therefore, the level 10 was adopted as the maximum division level.

Table 1. Values of drag coefficient for different levels.

Level	5	6	7	8	9	10	11
$\overline{C_d}$	0.6990	0.6813	0.6864	0.6932	0.6775	0.6595	0.6579
$\Delta\%$	6.28%	3.57%	4.33%	5.37%	2.98%	0.24%	0%

2.5. Method Validation

In this part, the flow past a sphere with different Reynolds numbers between 40 and 500 is calculated, and the drag and lift coefficients are analyzed and compared with other literatures. In Table 2, $\overline{C_d}$ and $\overline{C_L}$ represent the average drag coefficient and lift coefficient, respectively. S_t is the simplification of the Strouhal number.

$$C_d(t) = \frac{F_d(t)}{\frac{1}{2}\rho U_\infty^2 S}, C_L = \frac{F_L(t)}{\frac{1}{2}\rho U_\infty^2 S} \quad (5)$$

Table 2. Comparison of flow parameters over a sphere with Reynolds number $Re = 300$.

References	$\overline{C_d}$	$\overline{C_L}$	S_t
Mimeau et al. [6]	0.673	0.066	0.133
Johnson and Patel [7]	0.657	0.069	0.137
Tomboulides and Orszag [23]	0.671	—	0.136
Constantinescu and Squires [24]	0.655	0.065	0.136
Kim and Choi [25]	0.657	0.067	0.134
Present	0.659	0.062	0.133

F_d, F_L are the drag and lift force acting on the sphere. S is the cross-section area of the sphere perpendicular to the direction of the incoming fluid, and $S = \pi d^2/4$, and

$$S_t = \frac{fd}{U_\infty} \quad (6)$$

where f is the shedding frequency of wake vortex, which can be obtained by Fourier transformation of the drag coefficient. Table 2 shows that the results in this paper are consistent with the data in the literature.

Brown and Lawler [26] had fitted with a large amount of experimental data to obtain the relationship between the time-averaged drag coefficient and Reynolds number:

$$C_d = \frac{24}{Re}(1 + 0.15Re^{0.681}) + \frac{0.407}{1 + \frac{8710}{Re}}, Re < 2 \times 10^5 \quad (7)$$

Continue to use this algorithm to simulate the flow past the sphere under other Reynolds numbers, and then compare the data with the empirical formula to get Figure 2. The results are in good agreement with the empirical formula. The error between the two does not exceed 3%.

2.6. Flow Separation

In the Cartesian coordinate system, the angle between the intercepted slice plane and the positive axis of the y axis is set as α , $\alpha \in [0, \pi)$. The surface of the sphere forms a circle in this plane, and any point on the circle is $P(x, y, z)$. The angle between the OP and the positive axis of the x -axis is set as θ , $\theta \in [0, 2\pi)$. The radius of the sphere is R , as shown in Figure 3a. There are two separation points in each slice as shown in the Figure 3b; these are θ_1 and θ_2 . They are called upper separation points and lower separation points. The angle between them and the positive axis of the x -axis is called the upper separation angle and the lower separation angle, respectively.

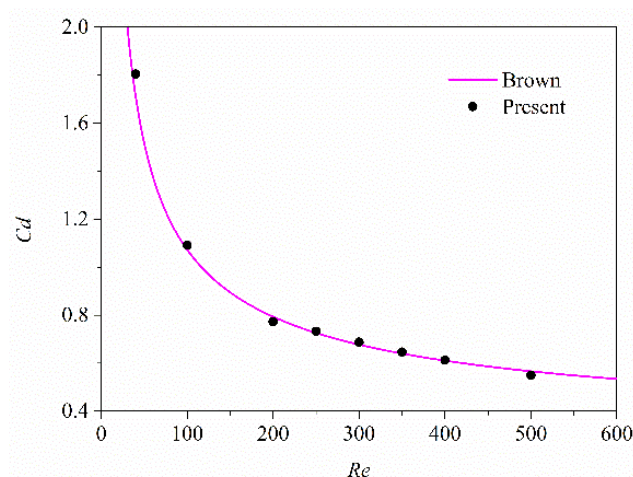


Figure 2. Comparative diagram between simulation results and the empirical formula.

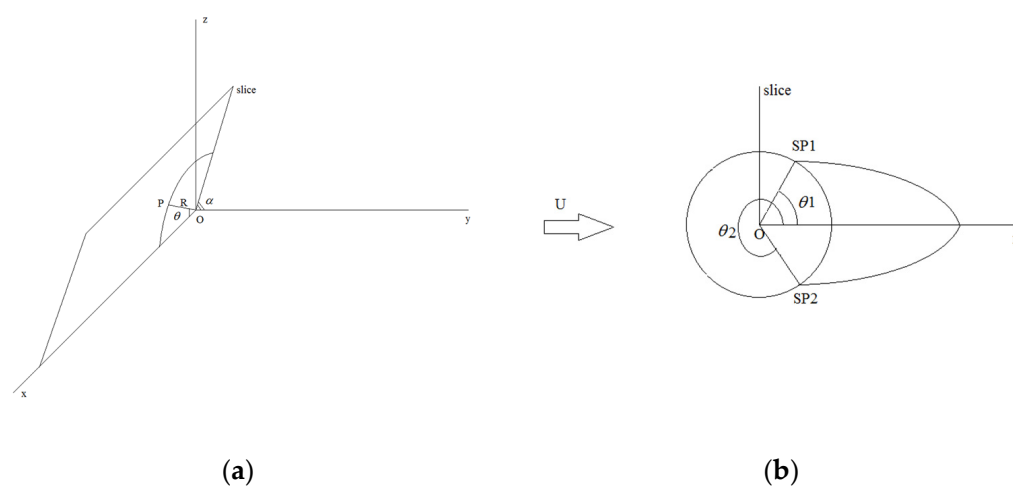


Figure 3. Schematic representation of various variables (a) and schematic diagram of separation points and separation angles (b).

2.6.1. To Extract the Separation Points from the Vorticity of the Points on the Surface of the Sphere

The flow separation occurs when the vorticity at some point on the sphere is nearly equal to zero in the Reference [27]. In addition, when the Reynolds number is equal to 20, there is no flow separation in the flow around the sphere, as shown in Figure 4a. With the increase of Reynolds number, the vorticity magnitude increases correspondingly, and the curves are highly symmetrical on the surface of the sphere whether in XY-plane (Figure 5a) or XZ-plane (Figure 5b), especially when the Reynolds number is not more than 200. The Figure 4b shows the two turning points represented by θ_1 and θ_2 . The separation angle θ_1 increases gradually with the increase of Reynolds number, while the separation angle θ_2 is the opposite.

2.6.2. Separation Angles Validation

In other references, the separation points are represented only by the upper separation points in the text, so only θ_1 is compared with others in Table 3. With the increase of Reynolds number, the separation angle increases gradually. Moreover, the calculated results are highly consistent with the data in the literature.

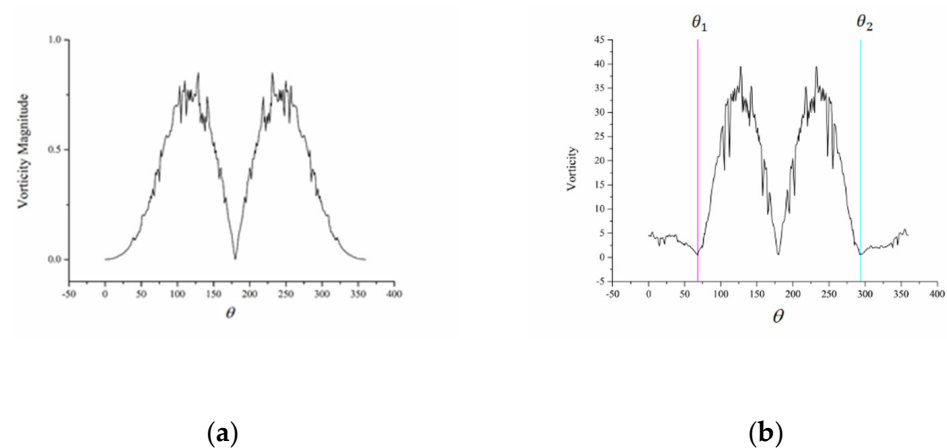


Figure 4. The vortices vary with the position of the sphere surface at $Re = 20$ (a) and $Re = 300$ (b) in XY-plane.

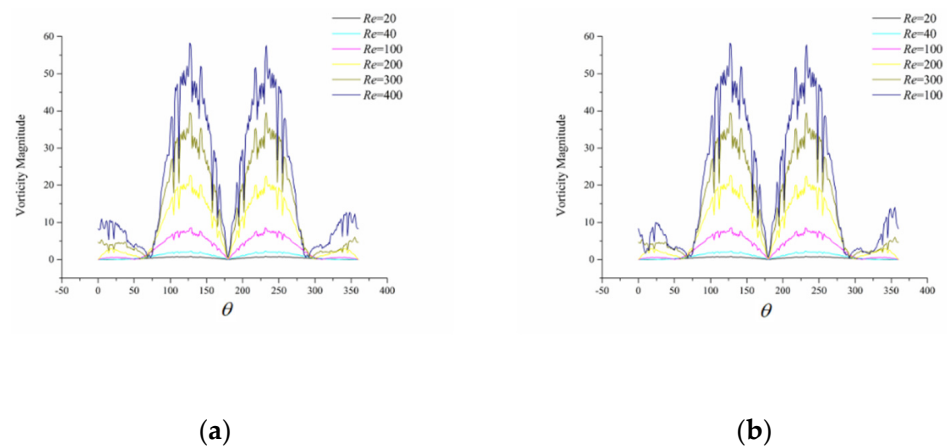


Figure 5. The vortices vary with the cycle position of the sphere surface for various Reynolds numbers at the same moment ($t = 65$ s). The left one (a) represents vortices on the sphere in XY-plane, and the right one (b) shows vortices in XZ-plane.

Table 3. Separation angles θ_1 ($^\circ$) compared with other references.

Re	40	100	200	300
Lee [9]	~	51	61	65
Kalra and Uhlherr [14]	31	50	60.5	66
Taneda [13]	34	53	63	67
Rimon and Cheng [10]	~	53	64	68
Sadikin et al. [8]	~	37	57	67
Seeley et al. [15]	~	60	~	67
Taamneh [28]	33.3	50	62	~
Present	33	50	61	64~68

3. Results and Discussion

The results of the flow around a rigid sphere with Re between 20 and 400 are presented in the paper. They are concluded the streamlines, the trend of force coefficient and the vorticity distribution on the surface of the sphere, vortex shedding, and evolution details of flow separation.

3.1. Lift, Drag, Lateral Force Coefficients and Streamlines

Between the Reynolds numbers of about 20~210, the flow around the sphere is a steady axisymmetric separated flow [6]. A series of figures on the left (1) represent the streamlines of Reynolds numbers at 20, 40, 100, 200, 300, and 400. The fluid flows from left to right. When the Reynolds number is less than or equal to 200, the flow around the ball under these Reynolds numbers has the same topology but has different flow separation positions, vortex core positions and separation bubble length. In addition, the streamline diagram is basically the same in different planes. However, when the Re exceeds 300, everything is different, and it is no longer an axisymmetric structure. The pressure coefficient distribution, which is defined as $C_p = (P - P_\infty) / (0.5\rho U_\infty^2)$, was presented in Figure 6(1). When the Reynolds number is less than or equal to 200, the pressure distribution is highly symmetrical in the XY plane, and the negative pressure region expands gradually. This indicates that when the Reynolds number does not exceed 200, the centrifugal force produced by vortex rotation and the viscous force opposite to the radial pressure gradient cancel out each other. While the Reynolds number exceeds 200, the closed small blue cycles in the wake represent the least pressure cells, which correspond to the rotating center of the annular vortices. In these cases, the pressure distribution in the near wake is no longer symmetrical. This leads to the asymmetrical flow separation at $Re \geq 300$.

When the Reynolds number is less than 200, the force coefficients in the three directions are constant and straight, as shown in Figure 6(2). Moreover, the force coefficients in the Y direction and the Z direction are equal to 0, which indicates that the force worked on the sphere is highly symmetrical. The drag coefficient, lift coefficient, and lateral force coefficient show the trend of sine or cosine function in two periods at $Re = 300$. Among them, the change of lift and lateral force is completely synchronized, and it does not fluctuate up and down at 0, which indicates that the forces on the sphere are not symmetrical, which also corresponds to the asymmetric fluctuation of the upper and lower separation points. The phase difference between the resistance and the two is about 90 degrees. When the Reynolds number is equal to 400, the force coefficients in the three directions change quasi-periodically. Meanwhile, the time mean value of the force coefficients in the Y and Z is not equal to 0, which indicates that the shedding of the vortex has the characteristics of certain priority direction and irregular shedding and presents quasi-periodic shedding.

The phase difference between the lift and lateral coefficients can reflect the directional characteristics of the flow on the cross-section perpendicular to the direction of the incoming flow. The above Figure 6(3) are phase differences composed of lift coefficients in the Y direction and the lateral force in the Z direction. When the Reynolds number is under 200, the phase of the lift coefficient and the lateral force coefficient almost converge at the origin of the coordinate, that is, the lift coefficient and the lateral force coefficient are approximately equal to zero. When the Reynolds number is equal to 300, the phase reaches a certain direction and then returns to the oscillation, which indicates that the lift coefficient is inclined to a certain direction but oscillates periodically, and the direction of the oscillation is consistent with the direction when the oscillation started. This is due to the periodic shedding of the spherical wake vortex and the statistical symmetry of the wake vortex. When the Reynolds number is equal to 400, the phase of lift and lateral force coefficient fluctuates unsteadily in the third quadrant, indicating that the direction of vortex shedding begins to fluctuate in a certain range.

3.2. Vortex in the Wake Field

Vortices in the wake field after the sphere are presented in Figure 7, and two particles that are symmetrical about the coordinate origin are selected to show their motion trajectory. The vortices appear on the sphere at $Re = 200$, and only very small vortices enter the wake field. And vorticity components in the X direction fall off alternately in the pair at $Re = 300$, the positive and negative vorticity iso-surfaces with the same absolute value

develop backward in the way of position exchange. At this moment, the trajectories of the two particles are completely symmetrical, just as the Reynolds number is 200. However, when the Reynolds number is equal to 400, the flow is not symmetric about the XY plane or XZ plane, and the symmetry disappears. The vortex legs of the hairpin vortex are twisted. By comparing with the periodic shedding vortex structure, it is found that the vortex head of the hairpin vortex and the vortex leg of the main clip vortex become shorter. The wake behind the sphere presents an irregular phenomenon of confusion. The trace behind the sphere is irregularly distorted in three-dimensional space.

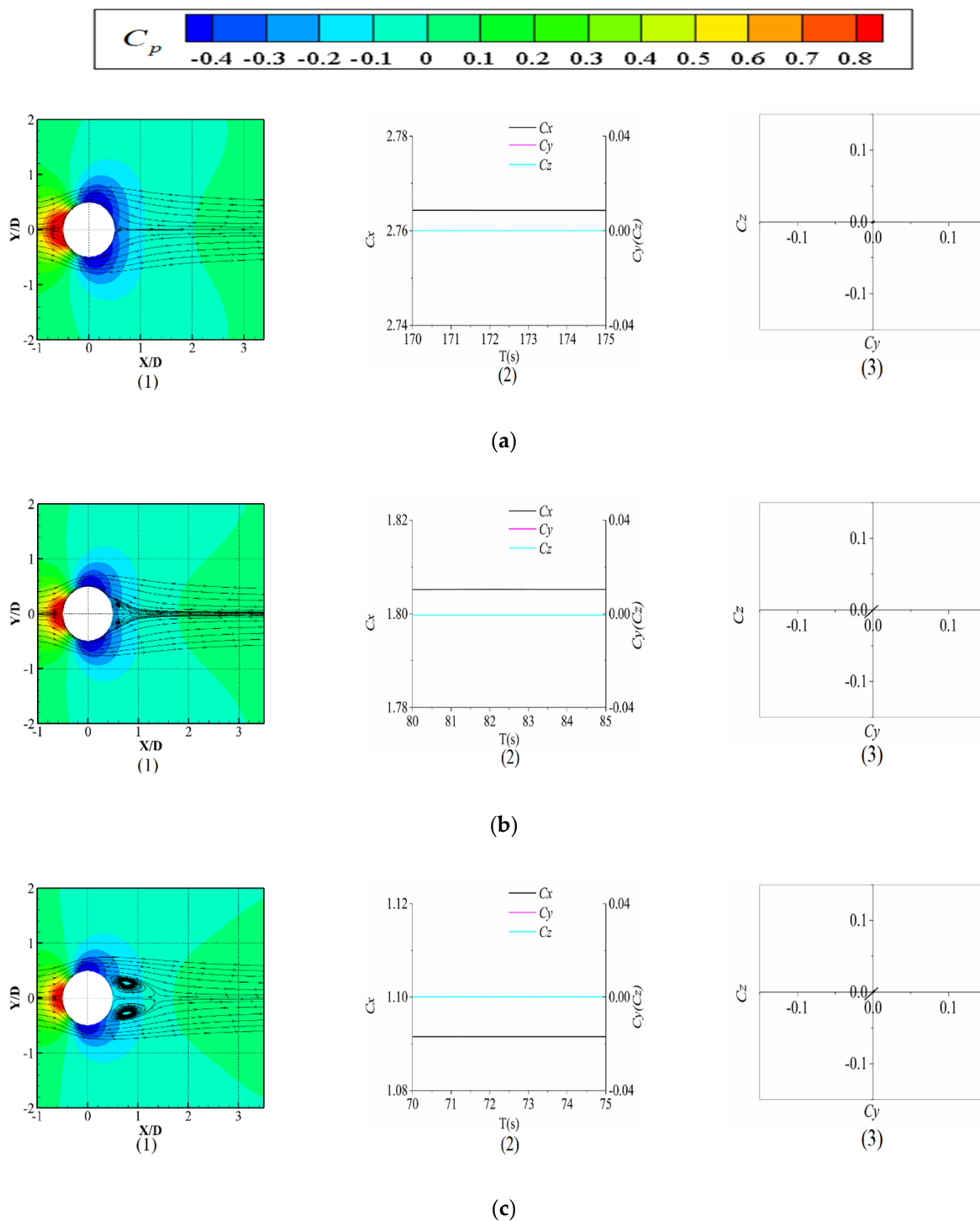


Figure 6. Cont.

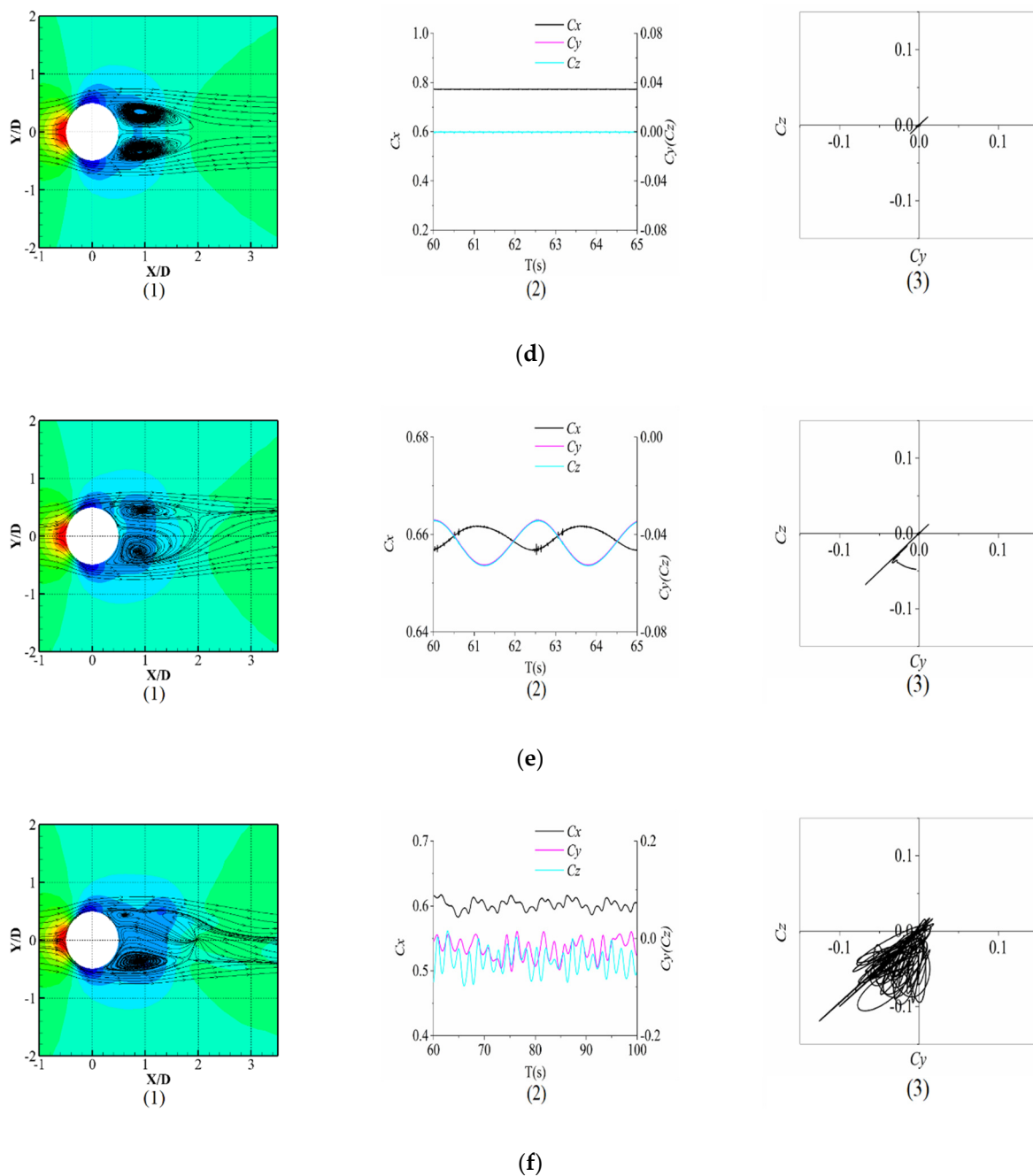


Figure 6. (1) Two-dimensional streamlines and pressure distribution in the near wake of flow around a sphere. (2) Force coefficients in three directions. (3) Phase diagram of force components in Y and Z directions at various Reynolds numbers: (a) $Re = 20$, (b) $Re = 40$, (c) $Re = 100$, (d) $Re = 200$, (e) $Re = 300$, and (f) $Re = 400$.

3.3. Time-Dependent Flow Separation

There is no flow separation when the Reynolds number is equal to 20. The flow is steady, and an axisymmetric separation bubble exists at the back of the sphere with zero lift and lateral force at $Re \leq 200$, and the two separation points are stable, and the flow separation is highly symmetrical. It can be seen from the following Table 4 that when the Reynolds number is not exceeding 200, the upper and lower separation points of the flow around the sphere are symmetrical about the x -axis. They fully satisfy the formula $\theta_1 + \theta_2 = 2\pi$. The separation angle θ_1 increases gradually with the increase of Reynolds number, while the separation angle θ_2 is the opposite.

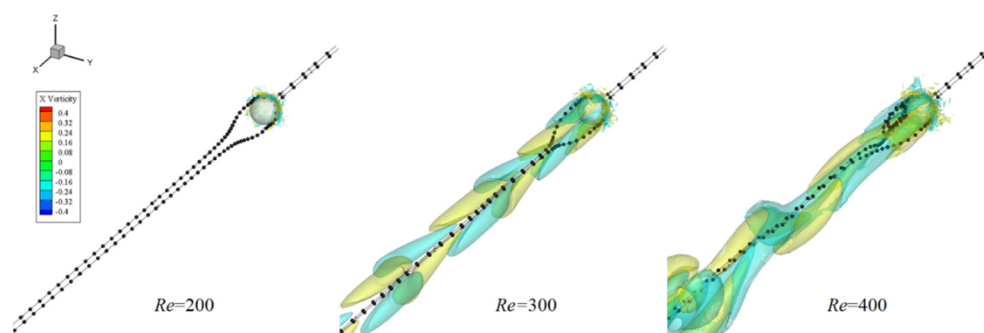


Figure 7. Iso-surface of vorticity component in flow direction and the trajectory of two fluid particles symmetrical about the origin after entering the field of flow around a sphere at different Reynolds numbers at $T = 65$ s. ($\omega_x = \pm 0.2$).

Table 4. Separation angles of flow separation of the sphere at various Reynolds numbers.

<i>Re</i>	20	40	100	200
$\theta_1(^{\circ})$	~	33	50	61
$\theta_2(^{\circ})$	~	327	310	299

It is illustrated here that the symmetric separation of flow around the sphere at the Reynolds number below 200 are similar, so only the time-dependent variation of the separation points at $Re = 200$ are presented in Figure 8. When the Reynolds number is equal to 200, the separation angles are stable with $\theta_1 = 61^{\circ}$, $\theta_2 = 299^{\circ}$.

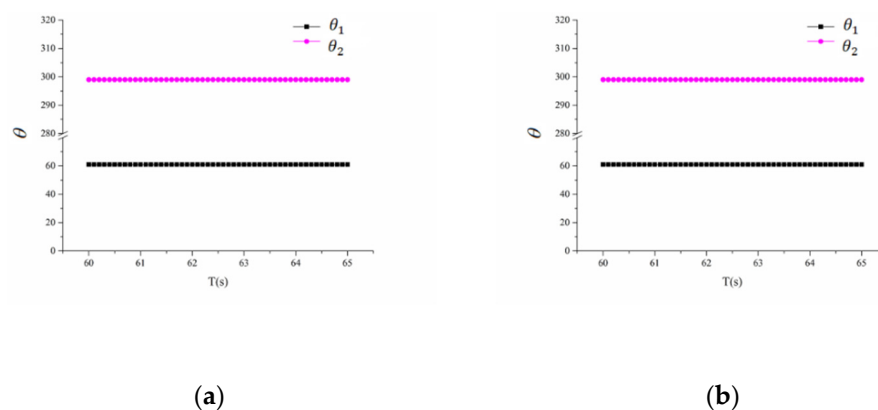


Figure 8. The time-dependent variation of separation angle over time in a period in XY-plane (a) and XZ-plane (b) at $Re = 200$.

When Reynolds number exceeds 300, both the period at $Re = 300$ and the quasi-period at $Re = 400$ are obtained from the Fourier transform of the drag coefficient. In two periods, the upper separation angle is very stable and remains 68 degrees in XY-plane (Figure 9a) and XZ-plane (Figure 9e). However, the lower separation angle fluctuates regularly in a certain small range. Moreover, the variation of the separation angles in the two planes are closely inlaid and echo each other, corresponding to the phase difference between the lift and the lateral force coefficient, which is manifested in a certain time difference. In other planes (Figure 9b,d,f,g), the two separation angles remain stable, except the planes of $\alpha = 45^{\circ}$ (Figure 9c) and $\alpha = 150^{\circ}$ (Figure 9h). Only in the slice of $\alpha = 45^{\circ}$, the upper separation angle fluctuates, and the lower separation angle remains stable, while it is the opposite in the slice of $\alpha = 150^{\circ}$.

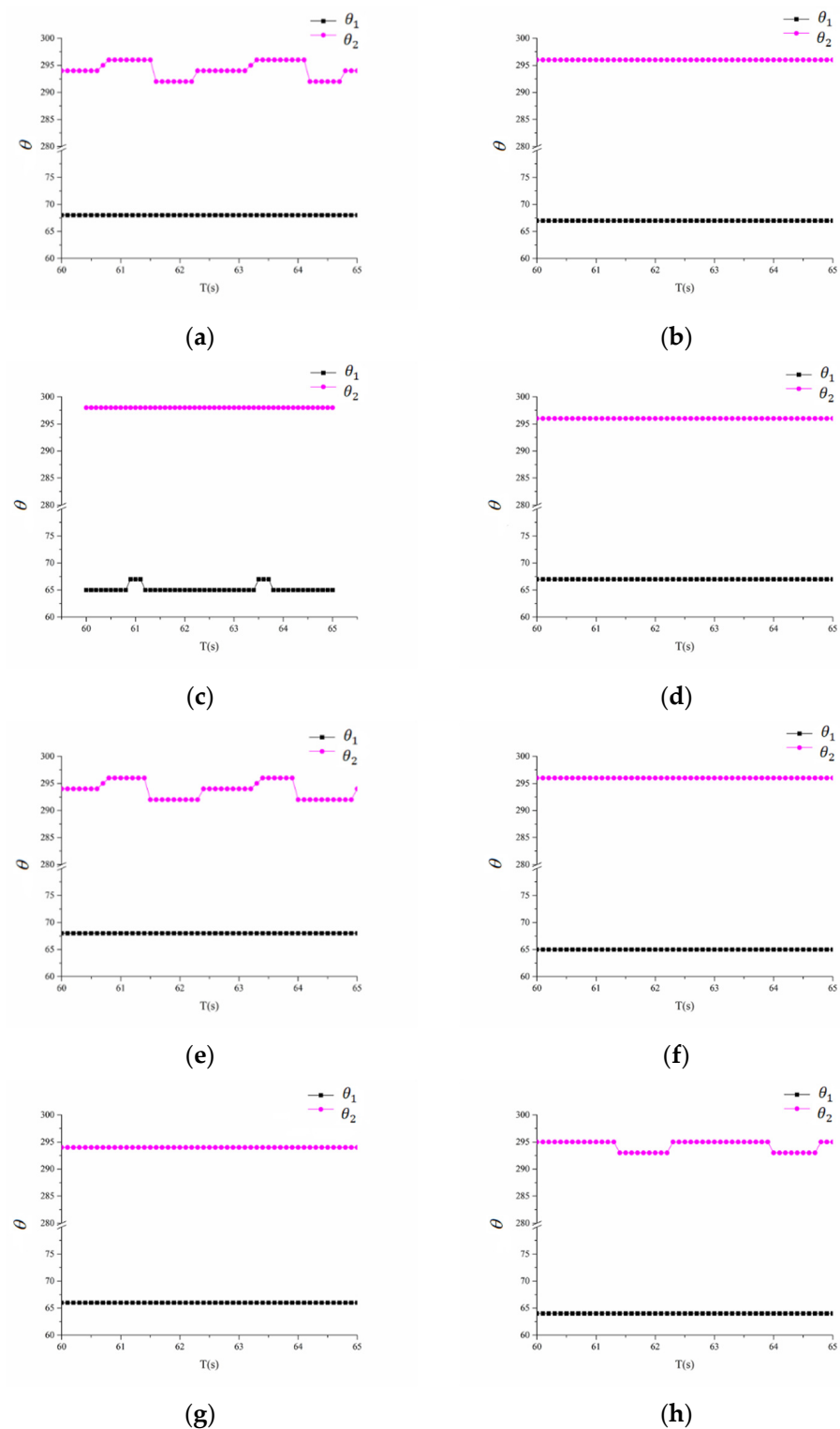


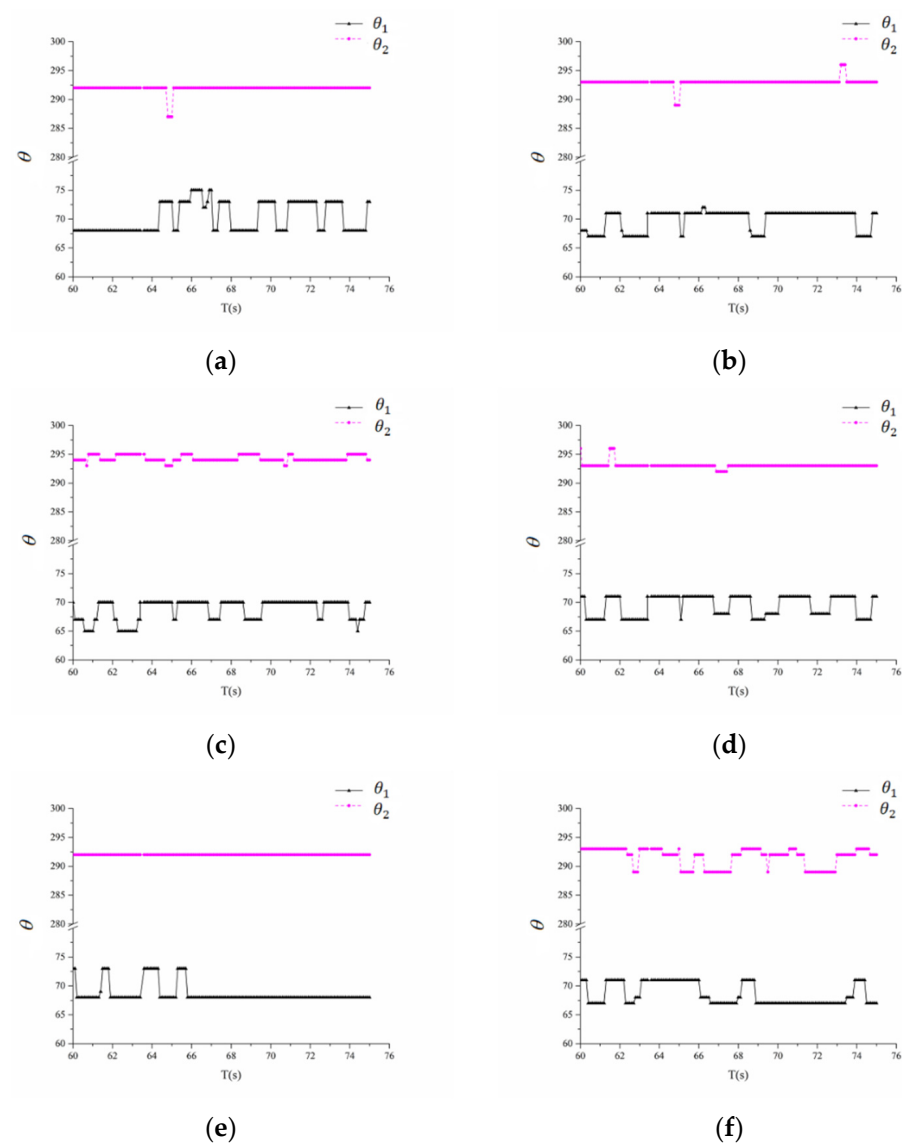
Figure 9. The time-dependent variation of separation angles in different planes during the two periods at $Re = 300$. (a) $\alpha = 0^\circ$, (b) $\alpha = 30^\circ$, (c) $\alpha = 45^\circ$, (d) $\alpha = 60^\circ$, (e) $\alpha = 90^\circ$, (f) $\alpha = 120^\circ$, (g) $\alpha = 135^\circ$, and (h) $\alpha = 150^\circ$.

The separation angles on different slices are similar in values, but different in variation at $Re = 300$. As shown in Table 5, the lower separation angles fluctuate on slices at some angles while others are fixed. On slices at certain angles, the sum of the two separation angles is no longer a constant of 360 degrees, even two fixed separation angles. This indicates that the flow separation is already asymmetric.

Table 5. The variation of separation angles in different slices when $Re = 300$.

$\alpha(^{\circ})$	0	30	45	60	90	120	135	150
$\theta_1(^{\circ})$	68	67	65–67	67	68	65	66	64
$\theta_2(^{\circ})$	292~296	296	298	296	292~296	296	294	293~295

If the Reynolds number is equal to 400, the upper and lower separation points are in a fluctuating state, as shown in Figure 10. The lower separation angle remains basically stable in a plane of $\alpha = 0^{\circ}, 30^{\circ}, 60^{\circ}, 90^{\circ}$, but they are stable at different angles of separation. Compared to the case of $Re = 300$, the separation angle varies frequently and irregularly, similar to the lift and lateral force coefficients under this case. The asymmetric fluctuation of the separation points corresponds to the irregular vortex falling in the wake field. Because data discretization points are extracted every 0.1 s, it is normal that data points jump a little.

**Figure 10.** Cont.

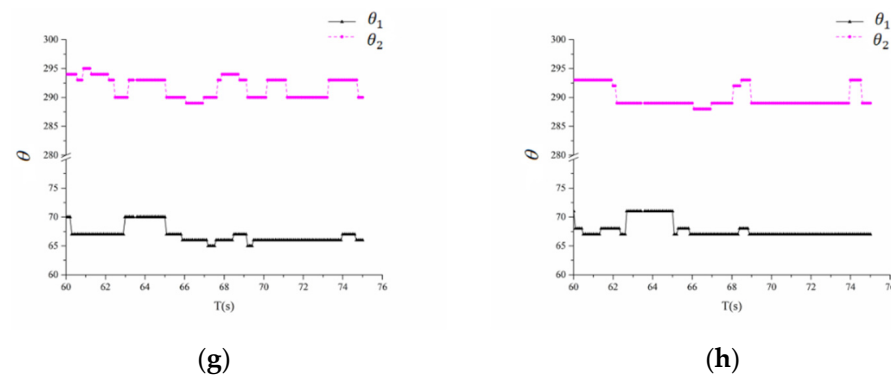


Figure 10. The time-dependent variation of separation angles in different planes during the two quasi-periods at $Re = 400$. (a) $\alpha = 0^\circ$, (b) $\alpha = 30^\circ$, (c) $\alpha = 45^\circ$, (d) $\alpha = 60^\circ$, (e) $\alpha = 90^\circ$, (f) $\alpha = 120^\circ$, (g) $\alpha = 135^\circ$, and (h) $\alpha = 150^\circ$.

4. Conclusions

The results show that the flow separates early when the Reynolds number increases within a certain range $40 \leq Re \leq 200$. In this Reynolds number interval, the separation angles are very stable at the fixed Re . As the Reynolds number continues to increase within 400, the symmetry of the flow separation around a sphere is analyzed in detail, and the flow separation angles are no longer fixed and symmetrical. The flow separation state changes from stable to periodically regular separation until completely irregular separation. Under this condition, the vortex structure in the wake changes from symmetrical and stable structure to asymmetric periodic structure, and finally to asymmetric and quasi-periodical vortex structure.

1. The flow is unsteady and time-periodic at $Re = 300$. And the flow separation becomes regular fluctuations, and the separation angle is not fixed, which is in the form that one of the separation points is stable and the other one oscillates regularly, and at the moment, the vortex is periodically shedding, and the flow separation is asymmetric. This leads to the fact that the mean value of the lateral force is not equal to zero, and the phase difference between lift and lateral force coefficients is about 90 degrees.
2. The flow is unsteady, non-periodic, and fully asymmetric at $Re = 400$, as is the flow separation around the sphere. The drag coefficient is no longer a regular fluctuation. The two separation angles become extremely unstable and disordered with time, just like the curve of the lift and lateral force coefficients. Additionally, the flow separation is completely asymmetric, and the vortex is spiral shedding. At the same time, the drag coefficient changes quasi-periodically, and the phase difference of the lift and lateral force coefficients also shows an irregular change trend.

Author Contributions: J.L.: Conceptualization, Methodology, Software, and Writing—Original Draft Preparation. B.Z.: Visualization, Writing—Review and Editing, and Supervision. All authors have read and agreed to the published version of the manuscript.

Funding: This research is supported by the Specialized Research Fund of the National Key Laboratory of Transient Physics under Grant No KX21373.

Institutional Review Board Statement: Not applicable.

Informed Consent Statement: Not applicable.

Data Availability Statement: The data that support the findings of this study are available from the corresponding author upon reasonable request.

Conflicts of Interest: The authors declare no conflict of interest.

References

1. Chester, W.; Breach, D.R.; Proudman, I. On the flow past a sphere at low Reynolds number. *J. Fluid Mech.* **1969**, *37*, 751–760. [[CrossRef](#)]
2. Achenbach, E. Experiments on the flow past spheres at very high Reynolds numbers. *J. Fluid Mech.* **1972**, *54*, 565–575. [[CrossRef](#)]
3. Okamoto, S. Turbulent shear flow behind a sphere placed on a plane boundary. In *Turbulent Shear Flows 2*; Bradbury, L.J.S., Durst, F., Launder, B.E., Schmidt, F.W., Whitelaw, J.H., Eds.; Springer: Berlin/Heidelberg, Germany; New York, NY, USA, 1980; pp. 246–256.
4. Tsutsui, T. Flow around a sphere in a plane turbulent boundary layer. *J. Wind. Eng. Ind. Aerodyn.* **2008**, *96*, 779–792. [[CrossRef](#)]
5. Tiwari, S.S.; Pal, E.; Bale, S.; Minocha, N.; Patwardhan, A.W.; Nandakumar, K.; Joshi, J.B. Flow past a single stationary sphere, 2. Regime mapping and effect of external disturbances. *Powder Technol.* **2020**, *365*, 215–243. [[CrossRef](#)]
6. Mimeau, C.; Cottet, G.H.; Mortazavi, I. Direct numerical simulations of three-dimensional flows past obstacles with a vortex penalization method. *Comput. Fluids* **2016**, *136*, 331–347. [[CrossRef](#)]
7. Johnson, T.A.; Patel, V.C. Flow past a sphere up to a Reynolds number of 300. *J. Fluid Mech.* **2000**, *378*, 19–70. [[CrossRef](#)]
8. Sadikin, A.; Mohd Yunus, N.A.; Abdullah, K.; Mohammed, A.N. Numerical study of flow past a solid sphere at moderate Reynolds number. *Appl. Mech. Mater.* **2014**, *660*, 674–678. [[CrossRef](#)]
9. Lee, S. A numerical study of the unsteady wake behind a sphere in a uniform flow at moderate Reynolds numbers. *Comput. Fluids* **2000**, *29*, 639–667. [[CrossRef](#)]
10. Rimon, Y.; Cheng, S.I. Numerical solution of a uniform flow over a sphere at intermediate Reynolds numbers. *Phys. Fluids* **1969**, *12*, 949–959. [[CrossRef](#)]
11. Lin, C.L.; Lee, S.C. Transient state analysis of separated flow around a sphere. *Comput. Fluids* **1973**, *1*, 235–250. [[CrossRef](#)]
12. Lee, D.K.; Downie, M.J.; Bettess, P. An axisymmetric model of separated flow about a sphere using discrete vortices. *Int. J. Numer. Methods Fluids* **2010**, *12*, 809–823. [[CrossRef](#)]
13. Taneda, S. Experimental investigation wake behind sphere low Reynolds numbers. *J. Phys. Soc. Jpn.* **1956**, *11*, 1104–1108. [[CrossRef](#)]
14. Kalra, T.R.; Uhlherr, P.H.T. Geometry of bluff body wakes. *Can. J. Chem. Eng.* **1973**, *51*, 655–658. [[CrossRef](#)]
15. Seeley, L.E.; Hummel, R.L.; Smith, J.W. Experimental velocity profiles in laminar flow around spheres at intermediate Reynolds numbers. *J. Fluid Mech.* **1975**, *68*, 591–608. [[CrossRef](#)]
16. Karyagin, V.P.; Lopatkin, A.I.; Shvets, A.I.; Shilin, N.M. Experimental investigation of the separation of flow around a sphere. *Fluid Dyn.* **1991**, *26*, 126–129. [[CrossRef](#)]
17. Park, S.H.; Park, G. Separation process of multi-spheres in hypersonic flow. *Adv. Space Res.* **2020**, *65*, 392–406. [[CrossRef](#)]
18. Park, S.H.; Kim, J.; Choi, I.; Park, G. Experimental study of separation behavior of two bodies in hypersonic flow. *Acta Astronaut.* **2021**, *181*, 414–426. [[CrossRef](#)]
19. Verekar, P.K.; Arakeri, J.H. Three-dimensional flow separations on a rolling sphere. *Sadhana-Acad. Proc. Eng. Sci.* **2019**, *44*, 35. [[CrossRef](#)]
20. Popinet, S. Gerris: A tree-based adaptive solver for the incompressible Euler equations in complex geometries. *J. Comput. Phys.* **2003**, *190*, 572–600. [[CrossRef](#)]
21. Popinet, S.; Smith, M.; Stevens, C. Experimental and numerical study of the turbulence characteristics of airflow around a research vessel. *J. Atmos. Ocean. Technol.* **2004**, *21*, 1575–1589. [[CrossRef](#)]
22. Liu, H.; Zhou, B.; Liu, Z.; Ji, Y. Numerical simulation of flow around a body of revolution with an appendage controlled by electromagnetic force. *Proc. Inst. Mech. Eng. Part G J. Aerosp. Eng.* **2013**, *227*, 303–310. [[CrossRef](#)]
23. Tomboulides, A.G.; Orszag, S.A. Numerical investigation of transitional and weak turbulent flow past a sphere. *J. Fluid Mech.* **2000**, *416*, 45–73. [[CrossRef](#)]
24. Constantinescu, G.S.; Squires, K.D. LES and DES investigations of turbulent flow over a sphere. In Proceedings of the 38th Aerospace Sciences Meeting and Exhibit, Reno, NV, USA, 10–13 January 2000. [[CrossRef](#)]
25. Kim, D.; Choi, H. Laminar flow past a sphere rotating in the streamwise direction. *J. Fluid Mech.* **2002**, *461*, 365–386. [[CrossRef](#)]
26. Brown, P.P.; Lawler, D.F. Sphere Drag and Settling Velocity Revisited. *J. Environ. Eng.* **2003**, *129*, 222–231. [[CrossRef](#)]
27. Zhang, H.; Fan, B.C.; Chen, Z.H.; Dong, G.; Zhou, B.M. Open-loop and optimal control of cylinder wake via electromagnetic fields. *Chin. Sci. Bull.* **2008**, *53*, 2946–2952. [[CrossRef](#)]
28. Taamneh, Y. CFD simulations of drag and separation flow around ellipsoids. *Jordan J. Mech. Ind. Eng.* **2011**, *5*, 129–132.